

EECE 5554 Robotics Sensing and Navigation

Lab 4: Navigation with IMU and Magnetometer

Carlos Anzola

Abstract

This report investigates the effectiveness of a navigation stack integrating a BU-353N GPS and a VN-100 IMU/AHRS to enhance navigation accuracy through sensor fusion. The study evaluates individual and combined sensor performance in key navigation metrics such as heading estimation, forward velocity, and dead reckoning, while addressing data integration challenges. Calibration, filtering, and sensor fusion techniques were applied to optimize results, with specific attention to minimizing errors.

Methods

GPS & IMU Driver. The data collection driver integrates GPS and IMU inputs into a unified ROS-based system for synchronized data acquisition. A custom IMU driver parses VNYMR data, publishing 3-axis orientation, linear acceleration, angular velocity, and magnetic flux density with timestamps. Simultaneously, a GPS driver collects GPGGA data, extracting latitude, longitude, altitude, and converting them to UTM coordinates.

Data Collection. Data was collected using the NUance vehicle (Northeastern University's "car of the future") [1]. The GPS device was mounted on the vehicle's roof, while the IMU was fixed on the center console armrest, aligned as centrally and level as possible. Two driving patterns were performed:

- **Circular paths:** The car was driven in circular paths within the same location to gather data for magnetometer calibration.
- **Loop around Boston:** The car was driven in a designated loop to capture a representative set of navigation data under urban conditions. The route emphasized frequent turns to evaluate the impact of angular motion on localization accuracy over time.

To focus on core navigation data and reduce complexity in motion analysis, a two-dimensional plane motion assumption was made. While this assumption excludes certain dynamics from the analysis, it still provides valuable insights into the vehicle's position and heading changes over time.

To enhance the two-dimensional analysis, the driving route avoided roads with significant elevation changes, such as dips and slopes. Although the 2D scenario wasn't fully preserved due to imperfect road conditions, these decisions ensured that the collected data remained largely suitable for planar motion assumptions.

Magnetometer Calibration. Magnetometers are subject to various error sources that can significantly impact measurement accuracy. Sources of these errors include, but are not limited to, bias, scale-factors, cross-coupling, soft & hard-iron distortion, and random noise [2]. To simplify the calibration process, this study focuses on hard and soft iron (HSI) distortions only.

The magnetometer measurement model described in the IMU documentation [3] is the following:

$$m_c = S_I(\tilde{m} - b_{HI}) \quad (1)$$

Where:

$m_c \in \mathbb{R}_{3 \times 1}$: $m_c = \begin{bmatrix} m_{c_x} \\ m_{c_y} \\ m_{c_z} \end{bmatrix}$ is the measured magnetic field vector.

$S_I \in \mathbb{R}_{3 \times 3}$: $S_I = \begin{bmatrix} C_{00} & C_{01} & C_{02} \\ C_{10} & C_{11} & C_{12} \\ C_{20} & C_{21} & C_{22} \end{bmatrix}$ is the matrix containing the soft-iron distortion coefficients.

$\tilde{m} \in \mathbb{R}_{3 \times 1}$: $\tilde{m} = \begin{bmatrix} \tilde{m}_x \\ \tilde{m}_y \\ \tilde{m}_z \end{bmatrix}$ is the true magnetic field vector.

And $b_{HI} \in \mathbb{R}_{3 \times 1}$: $b_{HI} = \begin{bmatrix} b_{HI_x} \\ b_{HI_y} \\ b_{HI_z} \end{bmatrix}$ is the vector containing the hard-iron distortion coefficients.

However, in most cases where the IMU's pitch and roll angles remain within 5-10° of level, a 2D calibration is sufficient [3].

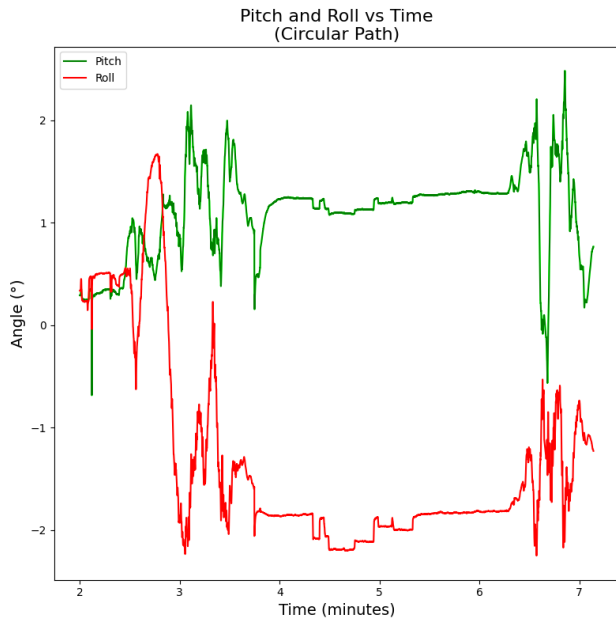


Figure 1. Pitch and Roll over Time in Circular Path.

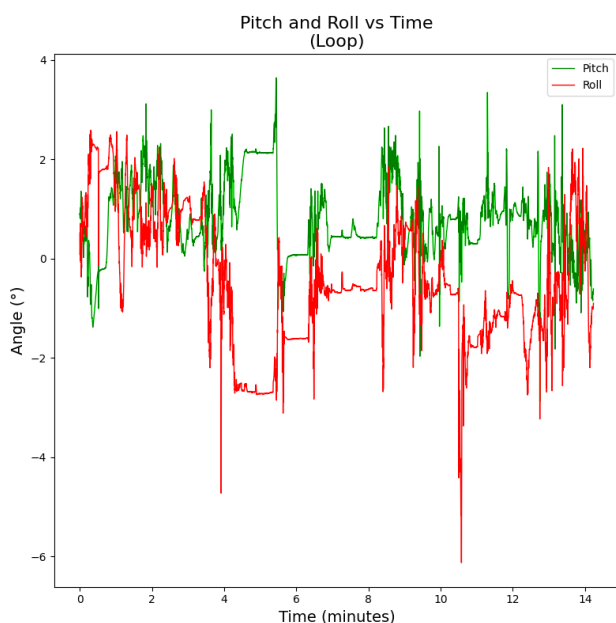


Figure 2. Pitch and Roll over Time during Loop.

As shown in Figures 1 & 2, the pitch and roll angles in both datasets stay within 10° of level. Therefore, a 2D HSI calibration was considered adequate for this analysis.

This assumption further simplifies the magnetometer measurement model described in Equation (1) to:

$$m_c = \begin{bmatrix} C_{00} & C_{01} & 0 \\ C_{10} & C_{11} & 0 \\ 0 & 0 & 1 \end{bmatrix} \begin{bmatrix} \tilde{m}_x - b_{HI_x} \\ \tilde{m}_y - b_{HI_y} \\ \tilde{m}_z \end{bmatrix} \quad (2)$$

Prior to the distortion coefficients calculation, outliers were removed using the *Isolation Forest* algorithm. This method was chosen for its effectiveness in detecting outliers in high-dimensional datasets without making any assumptions on the features' distribution [4].

Although the final calibration considers X and Y-axes only, the Isolation Forest algorithm was applied to the three axes to capture any irregularities across the entire magnetic field.

To obtain the distortion coefficients, least squares was used to fit an ellipse to the circular path data [5]. The ellipse fitting provided key parameters: the center point, lengths of the major and minor axes, and the orientation. These parameters were then applied in Equation (2) to derive a transformation matrix, which was used to correct the sensor readings as follows:

$$m_c = \begin{bmatrix} r \cos(\theta) & -\sin(\theta) & 0 \\ \sin(\theta) & r \cos(\theta) & 0 \\ 0 & 0 & 1 \end{bmatrix} \begin{bmatrix} \tilde{m}_x - c_x \\ \tilde{m}_y - c_y \\ \tilde{m}_z \end{bmatrix} \quad (3)$$

Where θ is the rotation of the ellipse with respect to the origin, r is the scaling factor obtained from the ratio between the semi major and minor axes, and (c_x, c_y) are the coordinates of the ellipse's centroid.

Heading Estimation. Heading estimation relied on both magnetometer readings and integrated gyroscope yaw rates. Given the nonlinear and noisy nature of these sensors, filtering was applied to enhance the signal quality and improve estimation accuracy. Before filtering, the Isolation Forest algorithm was employed to identify outliers in the data. The outliers were then substituted by an interpolated value from the neighboring data.

A Butterworth low-pass filter was applied to the magnetometer data to smooth out high-frequency noise while preserving the essential features of the signal. In contrast, a high-pass filter was applied to the gyroscope data to reduce the bias introduced by *Angle Random Walk* [3] over time.

To integrate both sensor readings, a complementary filter was implemented. This filter is defined in the IMU documentation as:

$$\theta_{k+1} = \alpha(\theta_k + \omega\Delta t) + (1 - \alpha)\theta_{accel} \quad (4)$$

Where θ_k and θ_{k+1} are calculated yaw angles, ω is the angular rate measured by the gyroscope, θ_{accel} is the pitch/roll angle derived from the accelerometer data, and α is the weight to adjust the contribution from each sensor [3].

To account for magnetometer data instead of accelerometer data, and to incorporate the gyroscope integration, this equation was modified as follows:

$$\theta_{k+1} = (\alpha)\theta_{gyro,k} + (1 - \alpha)\theta_{mag} \quad (5)$$

Where θ_{gyro} is the integrated value for the angular rate in degrees per second given by [6]

$$\theta_{gyro,k} = \sum_{i=1}^k \frac{\dot{\theta}_{i-1} + \dot{\theta}_i}{2} \Delta t_i \quad (6)$$

And θ_{mag} is the calculated yaw from the magnetometer data in degrees given by [7]

$$\theta_{mag} = \begin{cases} \tan^{-1}\left(\frac{m_{c,x}}{m_{c,y}}\right) + \delta, m_{c,y} \neq 0 \\ 180 + \delta, m_{c,y} = 0 \text{ and } m_{c,x} < 0 \\ 0 + \delta, m_{c,y} = 0 \text{ and } m_{c,x} > 0 \end{cases} \quad (7)$$

Where δ is the magnetic declination, which was assumed to be constant as its local variation falls within the order of a few hundredths of a degree. This value for the magnetic declination was obtained from the National Centers for Environmental Information's *Magnetic Field Calculators* [8].

In the updated equation, θ_{gyro} provides short-term responsiveness, which is critical during rapid movements or turns. Meanwhile, θ_{mag} contributes to long-term accuracy, helping to correct drift over time.

The optimal value for the cut off frequencies, filter order, and α were calculated using *Mean Square Error* (MSE) to minimize the error between the filtered data and the yaw from the IMU orientation. This approach ensures that the filters use optimal parameters and effectively balances the contributions of both sensors, maximizing heading estimation accuracy.

Forward Velocity Estimation. The forward velocity was estimated through two methods: integrating the forward acceleration from the IMU and calculating velocities directly from GPS data.

The equation describing the discrete integration of linear acceleration to obtain the forward velocity is the following:

$$v_{x,k} = \sum_{i=1}^k \frac{a_{x,i-1} + a_{x,i}}{2} \Delta t_i \quad (8)$$

The forward velocity from GPS data was obtained using GeoPy's geodesic function [9] which follows the method described in [10].

The accuracy of integrated accelerometer data is influenced by various error sources, particularly *Velocity Random Walk* (VRW), which appears as a drift over time. Additionally, accelerometer measurements are affected by bias originating from thermal, physical, mechanical, and electrical factors [3]. To reduce the impact of these errors, the following corrections were made:

- **Bias:** Since the vehicle was either stationary or moving forward during the loop dataset collection, the minimum expected velocity should be zero. However, the data displayed a negative minimum velocity. To correct this, the dataset was adjusted upward by the absolute value of this minimum velocity.
- **Drift:** Two steps were done to address the continuous drift. First, a high-pass filter was applied to the integrated forward acceleration to reduce the impact of VRW. Second, stationary timestamps were identified based on the GPS velocity calculations. The velocities at timestamps corresponding to stationary periods, along with subsequent ones, were adjusted by the velocity value recorded at the stationary timestamp.

- **Jump Correction:** Shifting different sections of the data introduced abrupt jumps in the velocity profile. To smooth these transitions, a Savitzky-Golay filter was applied. This filter uses a sliding window to fit the data to a polynomial through least squares, effectively smoothing out the jumps and creating a more continuous velocity profile.

Traveled Distance Estimation. The distance traveled was estimated by integrating the previously calculated forward velocities from the GPS and the IMU as follows:

$$d_{x,k} = \sum_{i=1}^k \frac{v_{x,i-1} + v_{x,i}}{2} \Delta t_i \quad (9)$$

Y-Axis Acceleration Estimation. To calculate the Y-axis linear acceleration, the following equation was used:

$$\ddot{y}_{obs} = \omega \dot{X} \quad (10)$$

Where \ddot{y}_{obs} is the measured Y-axis linear acceleration, ω is the angular velocity in the Z-axis, and \dot{X} is the X-axis integrated velocity from the accelerometer.

Trajectory Estimation. To find the trajectory using IMU data, the northing and easting velocities were calculated using the previously obtained forward velocity (8) and heading values (5) as follows:

$$\vec{v} = \begin{bmatrix} \vec{v}_e \\ \vec{v}_n \end{bmatrix} = v_x \begin{bmatrix} \sin(\theta) \\ \cos(\theta) \end{bmatrix} \quad (11)$$

Using this new velocity vector, Equation (9) was applied to obtain the trajectory of the vehicle.

$$\vec{x} = \begin{bmatrix} \vec{x}_e \\ \vec{x}_n \end{bmatrix} \quad (12)$$

Trajectory Alignment. For a proper comparison between the dead reckoning and GPS trajectories, the estimated trajectory from dead reckoning was rotated 62° counterclockwise to align with the orientation of the GPS trajectory. It was then scaled by factors of 0.735 and 0.79 along the X and Y axes, respectively. Additionally, the GPS trajectory was adjusted by shifting it according to the minimum easting and northing values to match the origin of the dead reckoning plot.

Results

The initial focus in heading estimation was calibrating the magnetometer to correct for hard-iron and soft-iron effects, which introduce distortions in magnetometer readings due to the presence of magnetic fields and ferromagnetic materials in the vehicle and surrounding environment.

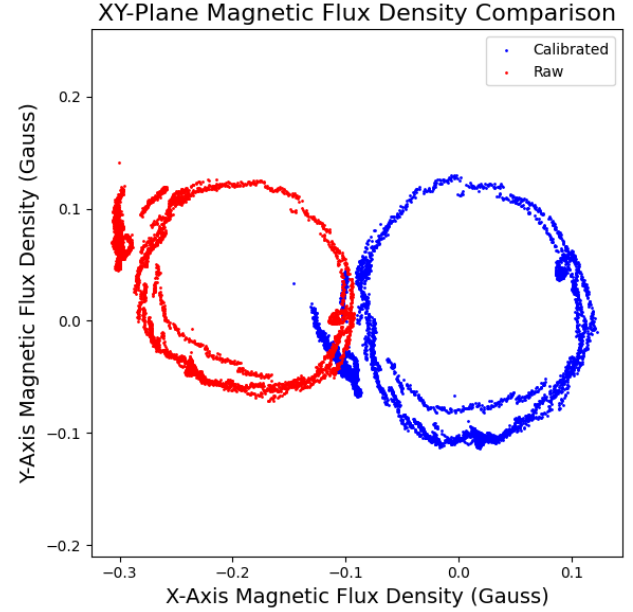


Figure 3. XY-Plane Magnetic Flux Density Comparison.

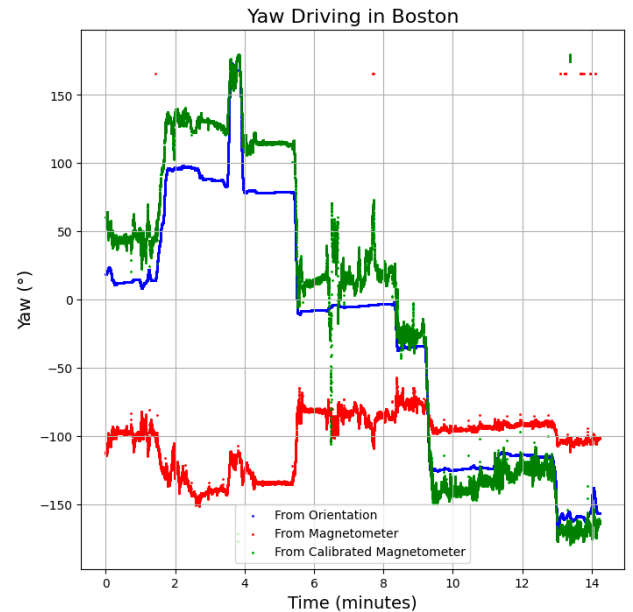


Figure 4. Yaw Estimation Before and After Magnetometer Calibration.

In Figure 3, distortions in the raw magnetometer data are evidenced as an elliptical pattern and an offset from the origin, which ideally should not appear in calibrated data. These features suggest the presence of hard and soft iron distortions. To address these distortions, the calibration values were computed using the method described in the *Magnetometer Calibration* section and applied to Equation (3). This process transformed the data into a state that more accurately depicts ideal measurement conditions.

In Figure 4, the effectiveness of the magnetometer calibration becomes more apparent. The uncalibrated heading data shows significant discrepancies when compared to the IMU's yaw orientation data, while the calibrated data more closely follows these values. Although the calibrated data does not completely align with the yaw data, it captures the main directional trends and accurately reflects vehicle turns, as indicated by the stepped pattern in the plot. However, it's important to note that discrepancies may persist due to the simplified measurement model, which does not account for a broader range of error sources, and because hard and soft-iron calibration does not correct for time-varying magnetic disturbances [3].

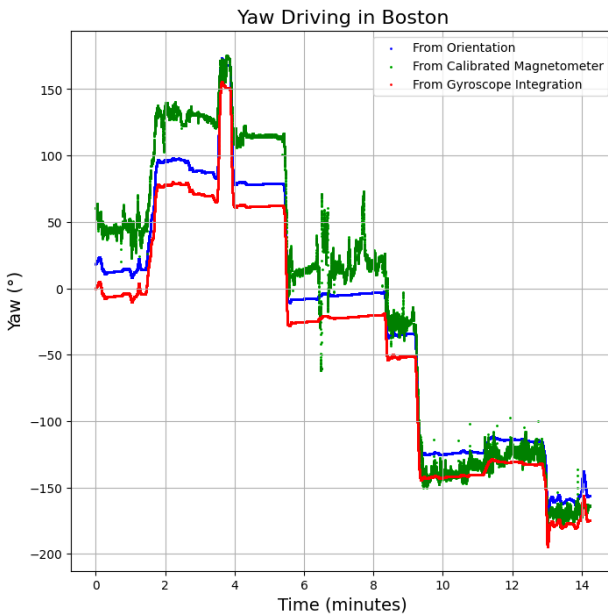


Figure 5. Gyroscope & Magnetometer Yaw Comparison.

Figure 5 presents a comparison between the ground truth yaw (computed by the IMU) and yaw estimates from both the calibrated magnetometer and the integrated gyroscope data. The gyroscope-based estimation shows less noise than the magnetometer and generally aligns well with the IMU yaw, though a slight bias is evident as a vertical shift. To reduce the impact of the previously mentioned errors in both sensors' data and improve estimation accuracy, a series of filters were applied.

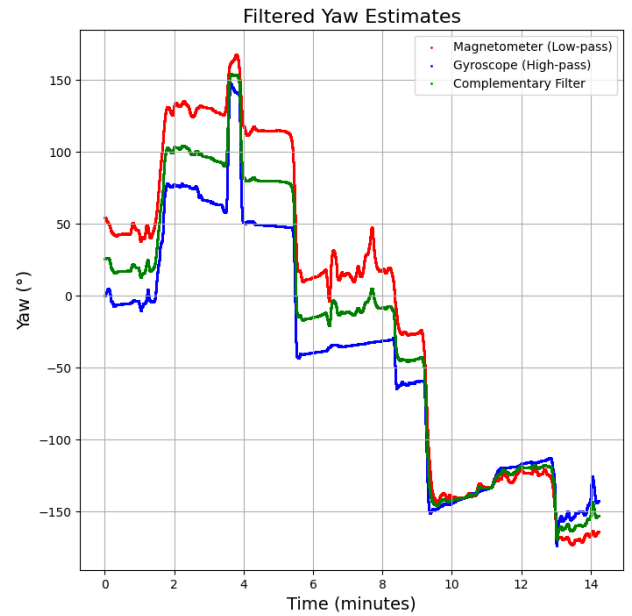


Figure 6. Filtered Yaw Comparison.

As shown in Figure 6, the low-pass filter applied to the magnetometer data effectively reduced signal noise, while the high-pass filter on the gyroscope yaw estimate minimized data drift, particularly noticeable towards the end of the dataset. By adjusting the cutoff frequency, order, and alpha value of the filters, the complementary filter successfully balanced responsiveness with noise reduction, producing a smooth and accurate yaw estimate. This approach allowed the complementary filter to maintain stability over time, effectively minimizing both the drift observed in the gyroscope data alone and the noise sensitivity of the magnetometer.

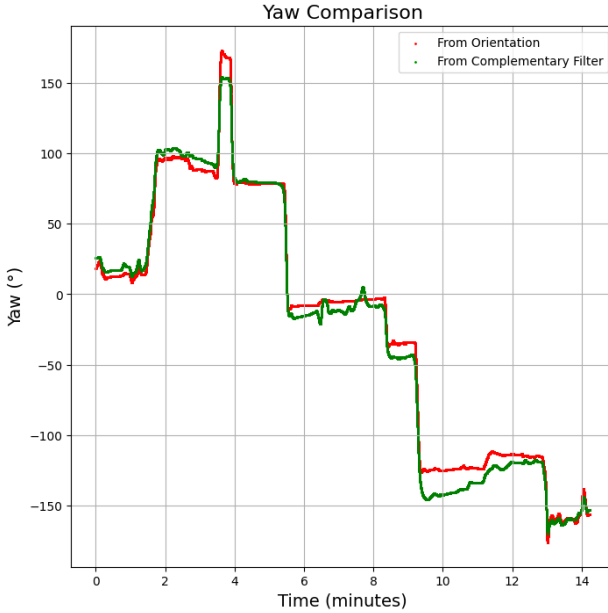


Figure 7. Yaw After Complementary Filtering.

This filtered yaw estimate, displayed alongside the IMU yaw in Figure 7, demonstrated superior reliability. Given its ability to consistently capture rapid directional changes while maintaining a stable average orientation, this estimate is recommended as the most suitable yaw estimate for vehicle navigation.

The calculated optimal values for the cutoff frequencies, filter order, and alpha coefficient are shown in Table 1.

Filter Type	Cutoff Freq. (Hz)	Order	α
Low-Pass	1.35	1	-
High-Pass	0.0009	5	-
Complementary	-	-	0.533

Table 1. Filter Parameters.

Estimating forward velocity required a combination of IMU data for the velocity estimation, and GPS data as a ground truth reference, each with unique error characteristics. The IMU-derived forward velocity was initially obtained by integrating the forward acceleration data from the IMU over time. However, this resulted in a velocity profile that drifted significantly from the GPS-derived velocity due to accelerometer bias and cumulative integration errors.

A direct comparison of the IMU and GPS velocities highlights the discrepancies, particularly during stationary periods where the IMU velocity failed to settle to zero.

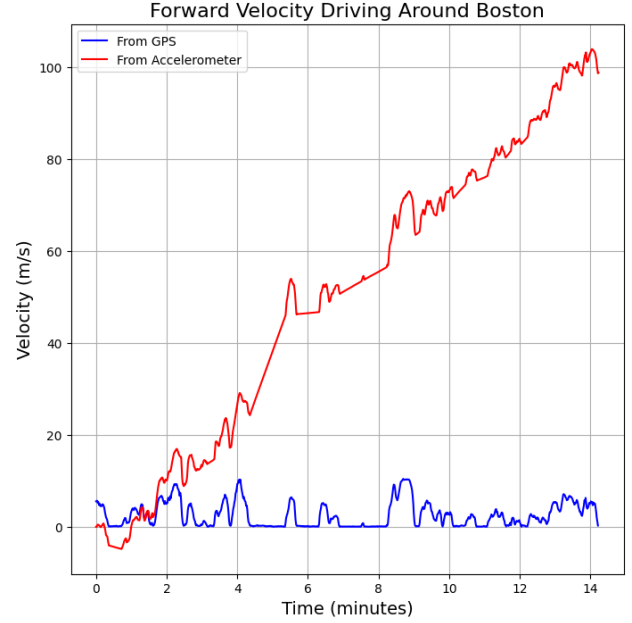


Figure 8. GPS & Accelerometer Velocity Comparison.

To correct for these errors, a baseline adjustment was performed, shifting the IMU-derived velocity to match the zero-velocity points identified in the GPS data. Furthermore, a high-pass filter was applied to the IMU data to counteract the influence of Velocity Random Walk (VRW). A Savitzky-Golay filter was also employed to smooth abrupt transitions, which appeared in the integrated acceleration data after the bias adjustments.

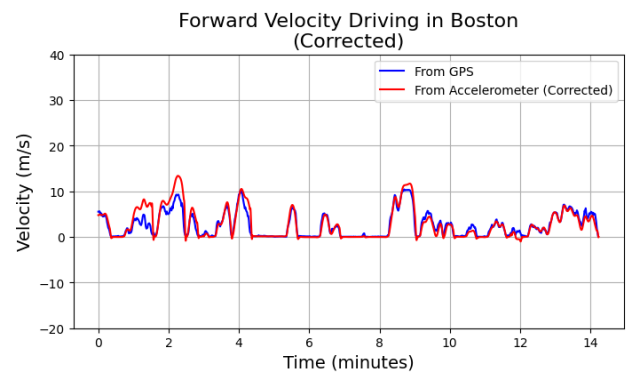


Figure 9. Corrected Forward Velocity from Accelerometer.

The comparison plot of corrected IMU velocity alongside GPS-derived velocity (Figure 9) showed much closer alignment, validating the corrections applied and confirming that, while IMU integration alone introduces drift, the adjusted IMU velocity can serve as a complementary estimate to GPS-derived velocity.

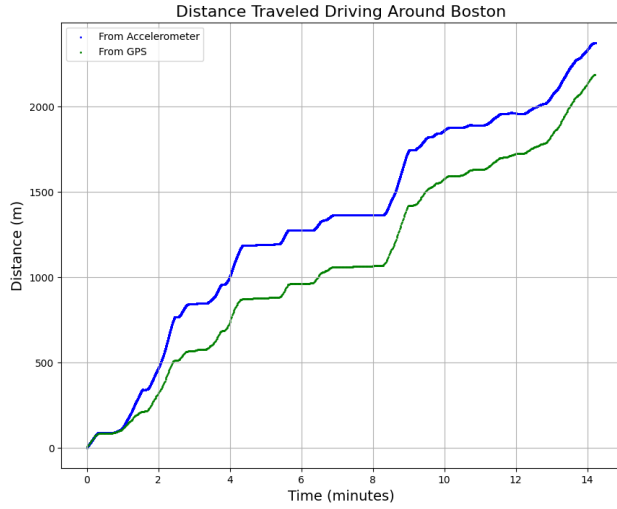


Figure 10. Estimated Distance Traveled from GPS & Accelerometer Data.

Figure 10 illustrates the traveled distance, revealing a clear distinction between the GPS estimates and the accelerometer-integrated values from the IMU. According to the specifications of the VN-100, in static conditions, the IMU should maintain reliable position estimates for about one minute, after which errors can exceed 40 meters [3] (likely greater in a dynamic condition). This expectation aligns with the observed data, as significant discrepancies between the GPS and IMU distance estimates began to show up even before the first minute elapsed. The substantial position error can be explained by Equation 3.17 in the VN-100 documentation, which indicates that position error is a non-linear function of time influenced by factors such as scaling, velocity error, bias, VRW, and ARW.

$$P_{err} = P_{err_0} + k\Delta P + V_{err_0}t + \frac{1}{2}b_a t^2 + \frac{2}{3}(\text{VRW})t^{\frac{3}{2}} + g \left[\frac{1}{6}b_g t^3 + \frac{4}{15}(\text{ARW})t^{\frac{5}{2}} \right]$$

Figure 11. Position Error from Equation 3.17 in the VN-100 Documentation.

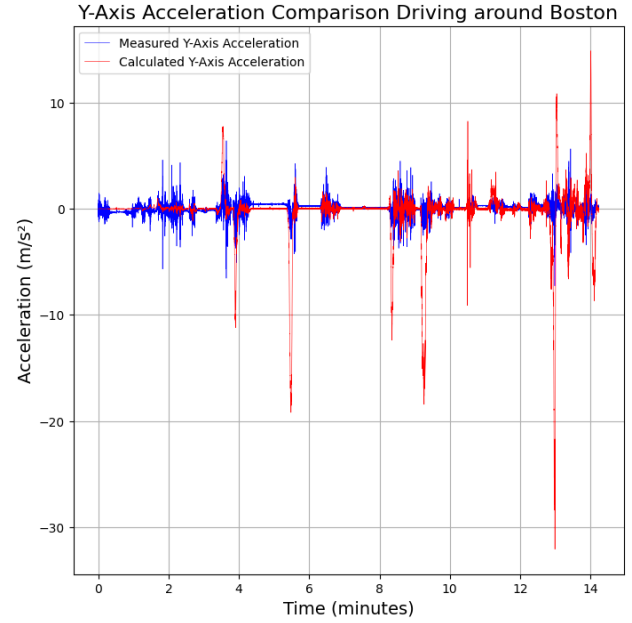


Figure 12. Measured & Calculated Y-Axis Acceleration.

To evaluate rotational and lateral acceleration consistency, the calculated lateral acceleration $\omega \dot{X}$ was compared with the observed \dot{y}_{obs} from the IMU. Figure 12 shows this comparison, indicating that both signals capture peaks associated with turns, and their baseline appear reasonably aligned during straight driving segments, though some differences show up due to high-frequency noise.

In a similar note to the previously mentioned position error sources, the VN-100 models the velocity error in Equation 3.14 of the IMU documentation [3] shown in Figure 13. From this equation, it can be noticed that scaling, bias, VRW, ARW, and the non-linear time-varying characteristics of the velocity error are also present in the velocity estimation. This is expected, as the position calculated previously is derived from the estimated velocity values, suggesting the propagation of error when integrating accelerometer data.

$$V_{err} = V_{err_0} + k\Delta V + b_a t + (\text{VRW})\sqrt{t} + g \left[\frac{1}{2}b_g t^2 + \frac{2}{3}(\text{ARW})t^{\frac{3}{2}} \right]$$

Figure 13. Velocity Error from Equation 3.14 in the VN-100 Documentation.

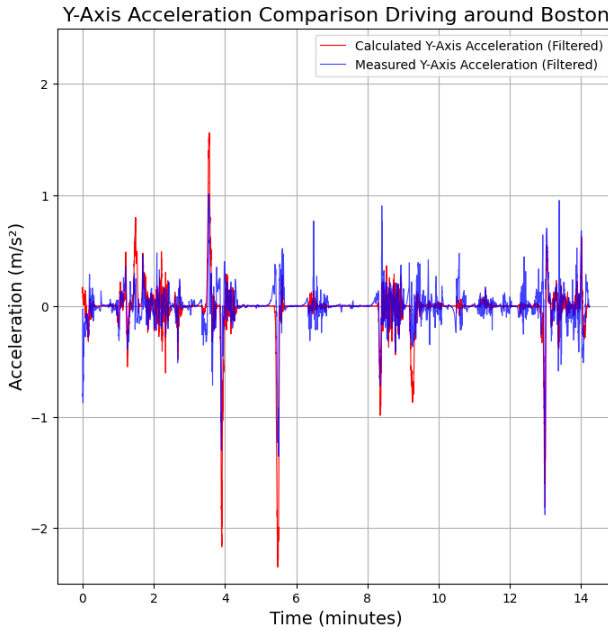


Figure 14. Measured & Filtered Calculated Y-Axis Acceleration.

Applying a band-pass filter of 1 – 15 Hz range on \ddot{y}_{obs} and following the correction steps for $\dot{\mathbf{X}}$ outlined in the *Forward Velocity Estimation* section considerably reduced the difference. This is further confirmed in Figure 14, which shows a better alignment after filtering the data.

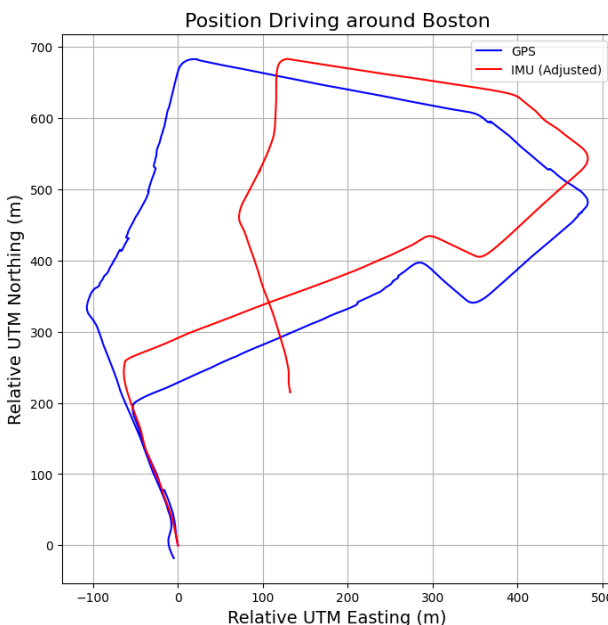


Figure 15. Dead Reckoning & GPS Trajectory Comparison.

While the adjusted IMU trajectory roughly follows the GPS trajectory shown in Figure 15, deviations begin to accumulate over time, especially noticeable after each turn. This increasing divergence reflects the limitations of dead reckoning through IMU integration, as small errors in orientation and velocity compound over time, causing a gradual drift. The deviations appear to amplify particularly during and after turning, likely due to the added complexity of accurately capturing rotational dynamics in the IMU data and in the proposed 2D dynamic model. This drift also results in a gradual distortion in distance estimates, indicating that even with initial alignment, long-term accuracy in IMU-only trajectory estimation is challenging without periodic corrections.

To conclude, while the IMU-based dead reckoning approach effectively captures the general trajectory pattern, its accuracy degrades over time due to cumulative integration drift, especially during turns and extended movements. Periodic recalibration with GPS data or advanced error-correction algorithms and filters could reduce this drift and improve the accuracy of IMU-derived trajectories.

References

- [1] P. Ramjug, "Students take a self-driving Lincoln out for a spin," *Northeastern Global News*, 2021.
- [2] D. N. P. P. S. Konstantinos Papafotis, "Magnetic Field Sensors' Calibration: Algorithms' Overview and Comparison," *Sensors*, vol. 21, no. 16, p. 5288, 2021.
- [3] VectorNav, "VECTORNAV," [Online]. Available: <https://www.vectornav.com/resources/inertial-navigation-primer/specifications--and--error-budgets/specs-magerrorsources>.
- [4] C. O'Sullivan, "datacamp," 25 September 2024. [Online]. Available: <https://www.datacamp.com/tutorial/isolation-forest>.
- [5] M. Sertic, "mirkosertic," 12 January 2023. [Online]. Available:

<https://www.mirkosertic.de/blog/2023/01/magnetometer-calibration-ellipsoid/>.

[6 Wikipedia, "Wikipedia," [Online]. Available:
] https://en.wikipedia.org/wiki/Trapezoidal_rule.

[7 Honeywell, "Adafruit," July 1995. [Online].
] Available: https://cdn-shop.adafruit.com/datasheets/AN203_Compass_Heading_Using_Magnetometers.pdf.

[8 National Centers for Environmental Information,
] [Online]. Available:
<https://www.ngdc.noaa.gov/geomag/calculators/magcalc.shtml#igrfwmm>.

[9 GeoPy, [Online]. Available:
] <https://geopy.readthedocs.io/en/stable/#module-geopy.distance>.

[1 "Algorithms for Geodesics," *Journal of Geodesy*, vol. 87, pp. 43-55, 2013.